




Ship Monitoring With Bistatic Compact HFSWR of Small Aperture

Yonggang Ji , *Member, IEEE*, Yiming Wang, *Member, IEEE*, Weifeng Sun , *Member, IEEE*, Ruifu Wang , Ming Li, Xiaoyu Cheng, and Xu Liang

Abstract—High-frequency surface wave radar (HFSWR) can detect and continuously track ship targets in real time and beyond the horizon. Compared with transmit/receive (T/R) monostatic HFSWR, the T-R bistatic HFSWR has the advantages of flexibility, receiver concealment, and large coverage because of the separation between the radar transmitter and receiver locations. So far, there is little research on marine ship monitoring for bistatic HFSWR. This article examines ship monitoring performance with T-R bistatic compact HFSWR of small aperture based on measured experimental data. The first-order sea-clutter characteristics and detection blind zone for T-R bistatic HFSWR were investigated theoretically, and the formulas for the moving ships were derived and its position accuracy were analyzed from simulation results. The experimental results of ship target detection of bistatic compact HFSWR carried out in 2015 were presented, and the spectrum characteristics of the bistatic HFSWR were analyzed with measured experimental data. A method integrating detection and tracking was applied to the target detection data collected by the bistatic compact radar, and two targets examples tracked were given. Finally, the validity of the method and the tracing results were verified by using synchronous automatic identification system data, and the ship positioning accuracy of the bistatic compact HFSWR was statistically analyzed. The analysis shows that bistatic radars have larger errors than monostatic T/R radars, with a positioning error as large as 10 km.

Index Terms—Automatic identification system (AIS), high-frequency surface wave radar (HFSWR), integrating detection and tracking, ship monitoring.

I. INTRODUCTION

HIGH-FREQUENCY surface wave radar (HFSWR), also known as HF surface over-the-horizon radar, operates in the 3–30 MHz band, with wavelengths between 100 and 10 m,

Manuscript received April 22, 2021; revised July 31, 2021 and December 21, 2021; accepted January 2, 2022. Date of publication January 11, 2022; date of current version January 21, 2022. This work was supported in part by the National Key R&D Program of China under Grant 2017YFC1405202, and in part by the National Natural Science Foundation of China under Grant 62031015. (Corresponding authors: Yonggang Ji; Ruifu Wang.)

Yonggang Ji, Weifeng Sun, Xiaoyu Cheng, and Xu Liang are with the College of Oceanography and Space Informatics, China University of Petroleum (East China), Qingdao 266580, China (e-mail: jiyonggang@upc.edu.cn; sunwf@upc.edu.cn; z20160009@s.upc.edu.cn; z20160026@s.upc.edu.cn).

Yiming Wang is with the Laboratory of Marine Physics and Remote Sensing, First Institute of Oceanography, Ministry of Natural Resources, Qingdao 26606, China (e-mail: wangyiming@fio.org.cn).

Ruifu Wang is with the College of Geodesy and Geomatics, Shandong University of Science and Technology, Qingdao 266590, China (e-mail: wrf@sdust.edu.cn).

Ming Li is with the College of Engineering, Ocean University of China, Qingdao 266100, China (e-mail: limingneu@ouc.edu.cn).

Digital Object Identifier 10.1109/JSTARS.2022.3142008

respectively. HFSWR can provide additional information on ship traffic, as it can detect ship targets over-the-horizon, has continuous-time coverage, and can estimate ship velocity through Doppler data [1], [2]. Compared with large-array HFSWR, compact HFSWR with small aperture occupies a smaller radar site, has lower power consumption, and is easier to deploy and maintain. Therefore, applications of compact HFSWR can be further expanded [3].

HFSWR can be categorized into monostatic radar systems and bistatic radar systems depending on the location configuration of the transmitting and receiving stations [4], [5]. In general, HFSWR works in monostatic transmit/receive (T/R) mode, where the transmitter antenna and receiver are colocated; T is the radar transmitter and R is the radar receiver. Monostatic T/R radar systems have many advantages, such as higher detection accuracy, simple technology implementation, and low cost. In T-R bistatic mode, the radar transmitter and receiver are installed at different locations far from each other. For bistatic T-R radar systems, the receiver is secure when the transmitter is attacked as the receiver is passive and in a state of concealment. Because the radar transmitter and receiver are positioned in separate locations, the receiving antenna or the transmitter can be placed on an island, an offshore platform or even a buoy or other mobile platforms, which can improve the detection range and flexibility of the radar system [6]–[8].

Moreover, as the receiving station and transmitting station are located at different sites, the receiving station can acquire additional target information at another observation view. Thus, moving targets originally buried in the sea clutter for T/R HFSWR can be separated from the sea clutter in the T-R bistatic HFSWR data. For this reason, bistatic T-R radar can be combined with monostatic T/R radar to form the T/R-R radar system; unlike the single monostatic or bistatic radar systems, the T/R-R system can obtain multidirectional observation information and improve ship target detection performances and precision [6], [9], [10], especially for the compact HFSWR system.

In addition, a bistatic HFSWR system has the potential to significantly improve the nighttime coverage area compared to a monostatic T/R radar system, while maintaining approximately the same daytime coverage. A bistatic system can also produce a higher radiated power aperture product from the same peak-power transmitter because it can use more efficient waveforms such as frequency-modulated continuous waves (FMCWs) [7]. However, bistatic HFSWR systems that employ FMCW waveforms may be more susceptible to other forms of ionospheric

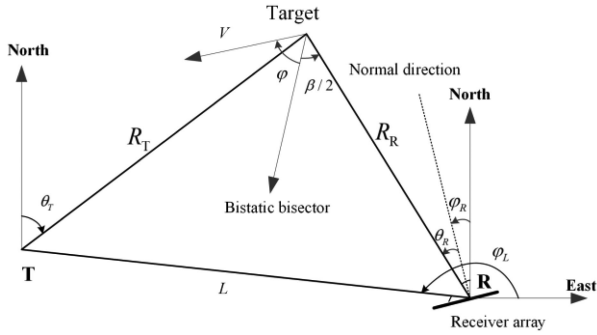


Fig. 1. Propagation path of a surface wave from a bistatic HFSWR.

clutter contamination (such as multiple round returns) and external interference [11].

Most articles on bistatic HFSWR focused on theoretical and simulation analysis. For example, Xie *et al.* [12] investigated the spreading mechanism of the first-order sea clutter for onshore bistatic HFSWR. Other articles based on measured HFSWR data mainly focused on analysis of the sea-clutter characteristic [13] and sea state monitoring, for example, Yang *et al.* [14] used a bistatic HFSWR to measure ocean currents. However, there is little research on marine ship target monitoring based on measured experimental data for bistatic compact HFSWR.

This article examines ship target monitoring with T-R bistatic compact HFSWR based on measured experimental data. The theoretical formulas of the first-order sea clutter and the target motion parameters are given in Section II. The target detection experiment using T-R bistatic HFSWR is introduced in Section III. Section IV presents the data processing algorithm for target monitoring which includes integrating detection and tracking for bistatic HFSWR. The tracking results are verified and the positioning accuracy is investigated in Section V. Finally, Section VI concludes this article.

II. SHIP TARGET PARAMETER ESTIMATION AND POSITION ERROR SIMULATION FOR BISTATIC HFSWR

A. First-Order Sea-Clutter Characteristics and Detection Blind Zone

Fig. 1 shows the scattered path of a bistatic HFSWR.

In Fig. 1, R_R is the range from the target to the receiving station **R**, R_T is the range to the transmitting station **T**, L is the distance between the transmitting station and receiving station, θ_R is the receiver look angle of the wave relative to the normal direction of the receiver, θ_T is the transmitter look angle of the wave relative to the north, and φ is the angle between the speed vector of the target and the bistatic angle bisector. φ_R represents the angle between the receiver array normal direction and the north, φ_L is the angle of the baseline relative to x -axis, and β is the bistatic angle. For the bistatic radar, the range that the radar measures directly are the sum of the ranges of the target relative to the transmitting station and that to the receiving station, i.e., $R = R_R + R_T$, the total scattered path. This range sum can locate the target on an ellipse whose two foci are at the location of the transmitter and receiver. The intersection of the estimated

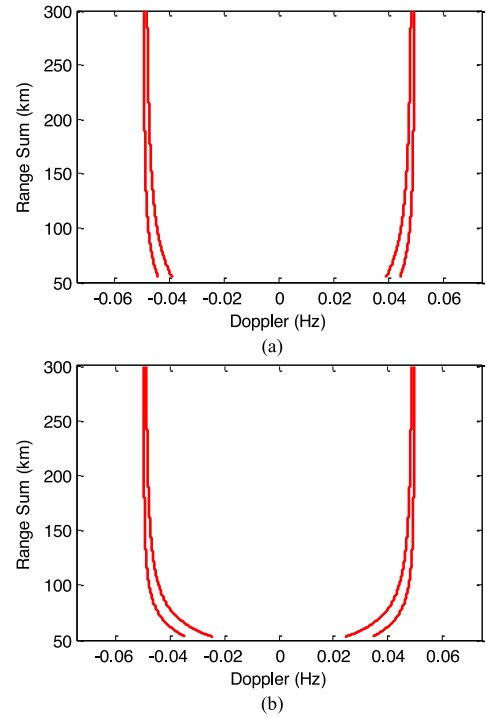


Fig. 2. Simulated result showing the velocity blind zone caused by the first-order sea clutter for bistatic HFSWR. (a) For a beam angle of -48° . (b) For a beam angle of 16° .

value of target's angle of arrival with the ellipse determines the location of the target. For HFSWR, the first-order sea clutter is the major interference source and creates detection blind zone in the radar echo spectrum. The Doppler shift of the first-order sea clutter for the bistatic HFSWR can be calculated in (1) [15]:

$$f_b = \pm \sqrt{\frac{g \cdot \cos(\beta/2)}{\pi\lambda}} + f_c \quad (1)$$

where λ is the radar wavelength, g is the gravity acceleration ($g = 9.81 \text{ m/s}^2$), and f_c is the Doppler frequency shift caused by the ocean current. According to (1), the first-order Bragg shift of a bistatic HFSWR is not fixed but a function of the bistatic angle β . It is also less than that of the monostatic T/R HFSWR, which can be expressed as $f_b = \pm \sqrt{\frac{g}{\pi\lambda}} + f_c$. Only when the bistatic angle β is close to zero at infinite distance, the Bragg frequency of the bistatic radar is equal to that of the monostatic T/R radar. The bistatic angle β is calculated using the formula:

$$\beta = \arccos\left(\frac{R_R^2 + R_T^2 - L^2}{2R_R R_T}\right). \quad (2)$$

Because of the wide beam of the HFSWR, the bistatic angle can vary within $[\beta_{\min}, \beta_{\max}]$, which can lead to a broadening of the first-order sea-clutter spectrum. The broad sea-clutter spectrum can further increase the range of the target detection blind zone. Fig. 2 gives two simulated range-Doppler (R-D) spectra with a beam direction of -48° and 16° off the boresight. In the simulation analysis, the same parameters as those of an actual HF radar system are used. The radar operating frequency is 4.7 MHz, the array comprises eight elements, 14.5 m apart, and the baseline distance between the transmitting station and

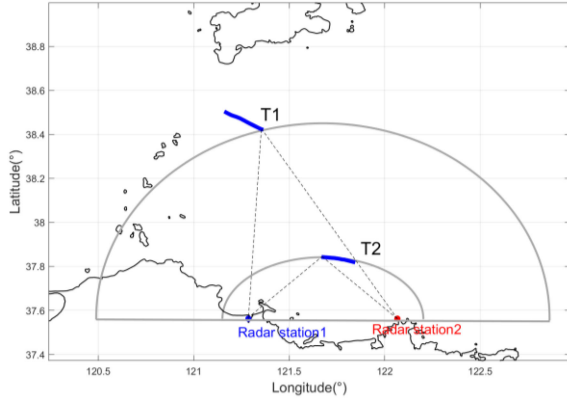


Fig. 3. Location of the two target tracks and radar stations.

the receiving station is 52.466 km. The target blind zone caused by the first-order sea-clutter spectrum appears for both radars.

In addition to the changes of the bistatic angle, the exiting and changing velocity of the ocean current v_c can also cause a shift and broadening of the first-order sea clutter of the bistatic HFSWR. The Doppler shift caused by ocean currents is

$$f_c = \frac{2v_c}{\lambda} \cos(\beta/2). \quad (3)$$

In the absence of tsunamis and other extreme marine events, the velocity of ocean currents is usually $v_c < 1$ m/s [16]. Therefore, the frequency shifts and the broadening of the first-order spectrum of the sea surface caused by ocean currents can be calculated by the maximum current velocity. Then

$$f_{c\text{Max}} = \frac{2v_{c\text{Max}}}{\lambda} \cos(\beta/2) = \frac{2}{\lambda} \cos(\beta/2). \quad (4)$$

Based on (1) and (4), it can be seen that the target detection blind zone caused by the first-order sea clutter for the T-R bistatic HFSWR is wider than that of the monostatic T/R radar, and is affected by factors such as the bistatic angle and ocean currents velocity.

B. Target Parameter Estimation for Bistatic HFSWR

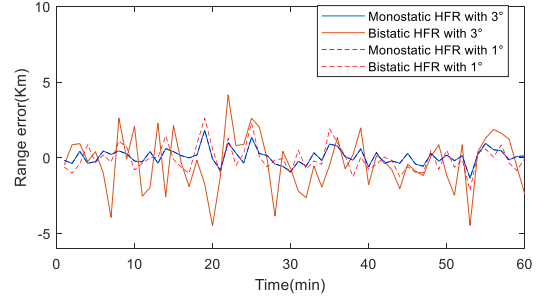
Based on the multichannel data acquired by the receiving station, the sum of the ranges R and the angles θ_R of the target relative to the receiving array can be obtained. According to the cosine theorem, the following relationship can be obtained:

$$R_T^2 = R_R^2 + L^2 - 2R_R L \cos \varphi_T. \quad (5)$$

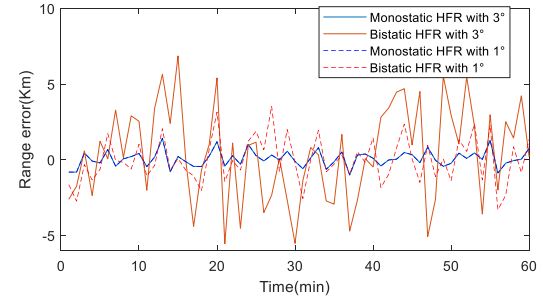
Here, $\varphi_T = \varphi_L - \varphi_R - \theta_R - \frac{\pi}{2}$, it can be set $\theta'_R = \varphi_L - \varphi_R - \theta_R$, then R_T and R_R can then be obtained by the following formula:

$$R_R = \frac{R^2 - L^2}{2(R - L \sin \theta'_R)}. \quad (6)$$

Thus, the target can be located by using obtained values of R_R and θ_R . The velocity obtained from the R-D spectrum of the bistatic HFSWR is the elliptical velocity relative to the reference ellipse on the bistatic angle, which is different from the radial velocity obtained from monostatic T/R HFSWR [17]. As seen

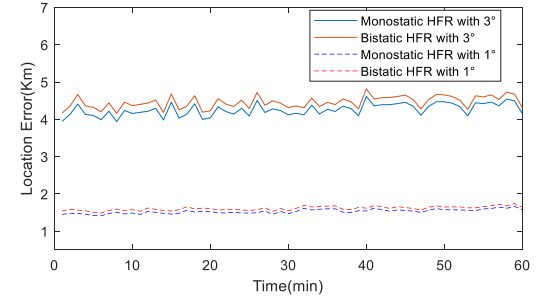


(a)

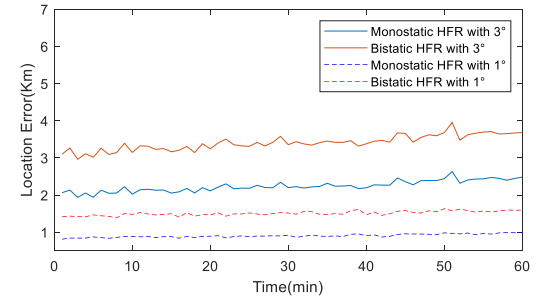


(b)

Fig. 4. Distribution curve of the target's range error. (a) Target 1. (b) Target 2.



(a)



(b)

Fig. 5. Target position error distribution curve (500 times average). (a) Target 1. (b) Target 2.

from Fig. 1:

$$\begin{cases} \frac{d}{dt} R_T = V \cos(\varphi - \beta/2) \\ \frac{d}{dt} R_R = V \cos(\varphi + \beta/2) \end{cases} \quad (7)$$

where φ is the angle between the speed vector of the target V and the bistatic angle. From this the formula of the elliptical velocity, V_E can be calculated as

$$V_E = \frac{d}{dt} R = \frac{d}{dt} R_T + \frac{d}{dt} R_R = 2V \cos \phi \cos \frac{\beta}{2}. \quad (8)$$

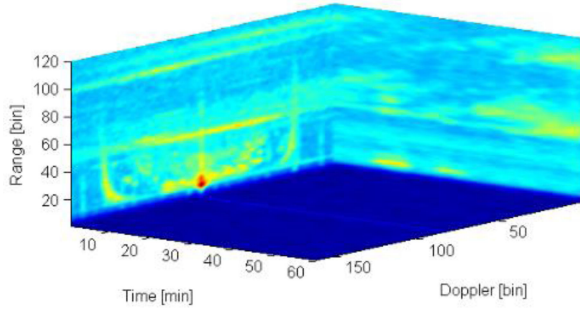


Fig. 6. R-D-T data of bistatic HFSWR.

As $\cos\beta = \frac{R_T^2 + R_R^2 - L^2}{2R_T R_R}$, then

$$\cos \frac{\beta}{2} = \sqrt{\frac{1}{2} + \frac{R_R - L\sin\theta'_R}{2\sqrt{R_R^2 + L^2 - 2R_R L\sin\theta'_R}}}. \quad (9)$$

The Doppler shift of the target can be obtained based on the known values of R_R and θ_R :

$$f_D = 2\frac{f_c}{c}V \cos\varphi \sqrt{\frac{1}{2} + \frac{R_R - L\sin\theta'_R}{2\sqrt{R_R^2 + L^2 - 2R_R L\sin\theta'_R}}}. \quad (10)$$

Setting $V' = V\cos\varphi$, the velocity of the target can be calculated by

$$V' = \frac{f_D c}{2f_c \sqrt{\frac{1}{2} + \frac{R_R - L\sin\theta'_R}{2\sqrt{R_R^2 + L^2 - 2R_R L\sin\theta'_R}}}}. \quad (11)$$

Because HFSWR can detect targets beyond the horizon, the target must be determined in spherical coordinates instead of plane coordinates when the target is far from the radar station. The formulas for converting the measurement parameters in spherical coordinates into that in plane coordinates can be expressed as [18]

$$\begin{cases} r = 2R_0 \sin(\frac{r'}{2R_0}) \\ \tan\varphi = \tan\varphi' \cdot \cos(\frac{\theta}{2}). \end{cases} \quad (12)$$

Here, R_0 is the earth radius, r and φ are the radial range and azimuth in the plane coordinate system, respectively, r' and φ' are the radial range and azimuth in the spherical coordinate system, respectively, and θ is the radian from r on the sphere. Therefore, the target distance, azimuth, and velocity of the bistatic HFSWR in the spherical coordinate system are

$$\begin{cases} r' = 2R_0 \arcsin(\frac{r}{2R_0}) \\ \varphi' = \arctan\left(\frac{\tan\varphi}{\cos(\frac{\theta}{2})}\right) \end{cases} \quad (13)$$

$$V' = \frac{f_D c}{2f_c \sqrt{\frac{1}{2} + \frac{r' - L\sin\theta'_R}{2\sqrt{r'^2 + L^2 - 2r' L\sin\theta'_R}}}}. \quad (14)$$

C. Simulation Analysis of Positioning Accuracy for Bistatic HFSWR

When the target range R and the receiving station azimuth θ_R have measurement errors of Δ_R and Δ_A , respectively, the actual

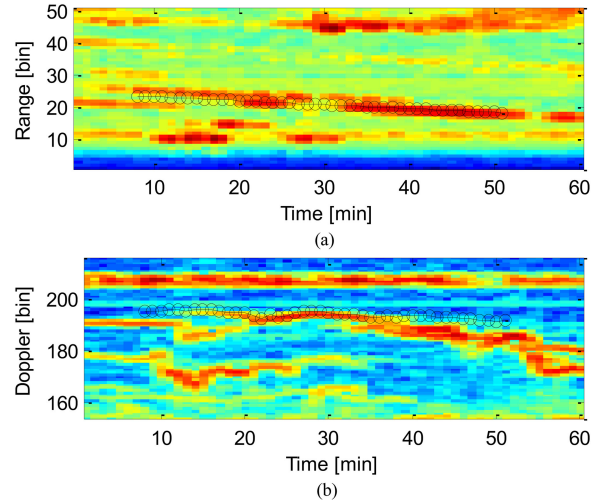


Fig. 7. R-T and D-T image and corresponding AIS data of target T1. (a) R-T image of T1 at the 192 Doppler bin. (b) D-T image of T1 at the 21 range bin.

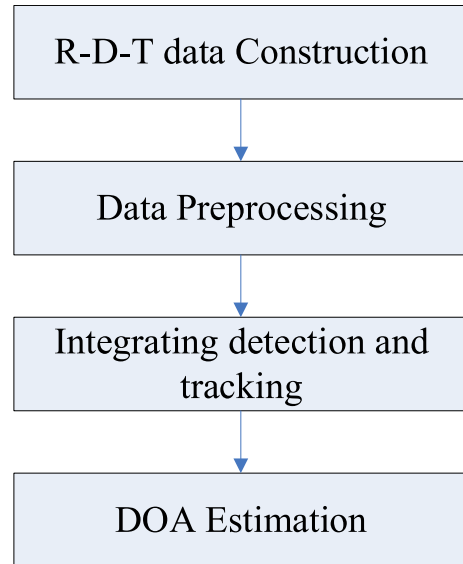


Fig. 8. Flowchart of the integrated detection and tracking process for bistatic HFSWR.

target range a and range error a' are expressed, respectively:

$$a = \frac{R^2 - L^2}{2(R - L\sin\theta'_R)} \quad (15)$$

$$a' = \frac{(R + \Delta_R)^2 - L^2}{2[R + \Delta_R - L\cos(\varphi_T + \Delta_A)]}. \quad (16)$$

Then, the range error R_{err} and spatial position error P_{err} are, respectively:

$$R_{err} = a' - a \quad (17)$$

$$P_{err} = c = \sqrt{a'^2 - a^2 - 2aa'\cos\Delta_A}. \quad (18)$$

When they are converted to spherical coordinates, they can be expressed as follows, respectively:

$$R_{err} = a' - a \quad (19)$$

$$P_{\text{err}} = R_0 \cdot \arccos \left(\cos \frac{a}{R_0} \cdot \cos \frac{a'}{R_0} + \sin \frac{a}{R_0} \cdot \sin \frac{a'}{R_0} \cdot \cos \Delta_A \right) \quad (20)$$

$$a = R_0 \cdot \arctan \left(\frac{\cos \frac{L}{R_0} - \cos \frac{R}{R_0}}{\sin \frac{R}{R_0} - \sin \frac{L}{R_0} \sin \theta'_R} \right) \quad (21)$$

$$a' = R_0 \cdot \arctan \left(\frac{\cos \frac{L}{R_0} - \cos \left(\frac{R+\Delta_R}{R_0} \right)}{\sin \frac{R}{R_0} - \sin \frac{L}{R_0} \cos(\varphi_T + \Delta_A)} \right) \quad (22)$$

It can be seen from the above formula that the spatial position error of the bistatic HFSWR is related to the range, range error, azimuth, and azimuth error of the target since its range is related to the target's azimuth (including azimuth error). The spatial positioning error of monostatic HFSWR is related to the target's range, range error, and azimuth error, but not to the target's azimuth.

To quantitatively evaluate the spatial position accuracy of bistatic HFSWR, two ship target trajectory results [from automatic identification system (AIS) data] are selected to analyze the statistical distribution results of the range the positioning error when they are given specific measurement errors, including range error and azimuth error. Fig. 3 shows the trajectories of the two targets and the locations of the transmitting and receiving stations. In which, the duration of the two target tracks is 1 h, one point per minute. The receiving station is located at (121.286E, 37.562N), while the transmitting station is located at (121.286E, 37.562N) (122.066E, 37.562N).

Figs. 4 and 5 show the distribution curves of the range error and position error of the two targets. In which, position error refers to the distance between the simulated tracking results of the bistatic compact HFSWR and AIS. To analyze the difference between the compact HFSWR and the large-array HFSWR, the azimuth errors Δ_A are, respectively, set to 3° and 1° , and the range error Δ_R is set to 1 km based on the actual radar measurement accuracy. In order to reduce the influence of system deviation, their average values were set to 0.

Fig. 4 shows that the range error of monostatic HFSWR is not related to azimuth since the curves of 3° coincide with those of 1° for two targets. While the range error of bistatic HFSWR is affected by the azimuth error. As a result, bistatic HFSWR has a substantially higher range error than monostatic HFSWR, and the bigger the azimuth error, the greater the range error. It is also influenced by the bistatic angle. So the range error of T2 is higher than that of T1 since the bistatic angle of T2 is obviously greater than that of T1.

It can be seen from Fig. 5 that the azimuth error has a significant impact on the target's position error of HFSWR, which is considerable for both monostatic and bistatic modes when the azimuth error is large. When the bistatic angle is small (T1), the position errors of monostatic and bistatic HFSWR are relatively close, and they are mainly determined by the azimuth error. As the influence of bistatic increases, the influence of range error of bistatic HFSWR increases, and the difference of position error between monostatic and bistatic begins to increase (T2).

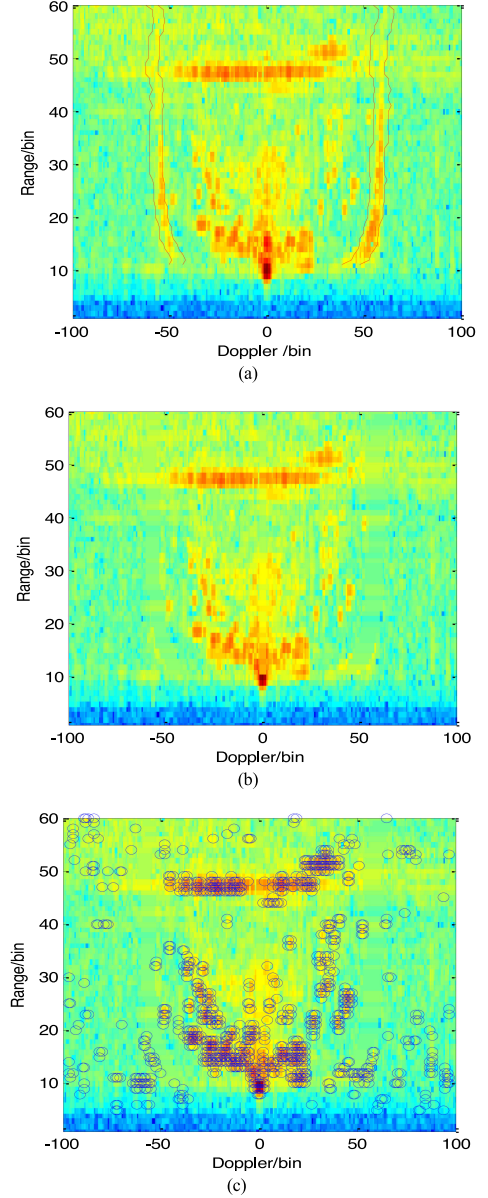


Fig. 9. First-order sea clutter extraction and suppression results. (a) Extraction. (b) Suppression. (c) CFAR predetection results.

III. SHIP TARGET MONITORING METHOD FOR BISTATIC HFSWR

In the traditional processing scheme of target monitoring with the large-array HFSWR, detection and tracking are two separate processes. Compared with the large-array HFSWR, the compact HFSWR has wider beam width and lower angle measurement accuracy. For a given moving target, wider beam width means lower signal-to-noise ratio (SNR) at a given beam angle, which will cause a lower detection rate and increase missing rate during the detection stage. Furthermore, a reduced detection rate and angle measurement accuracy can result in target track fragmentation or loss during the tracking stage. As a result, the typical tracking after detection technique is ineffective for compact HFSWR.

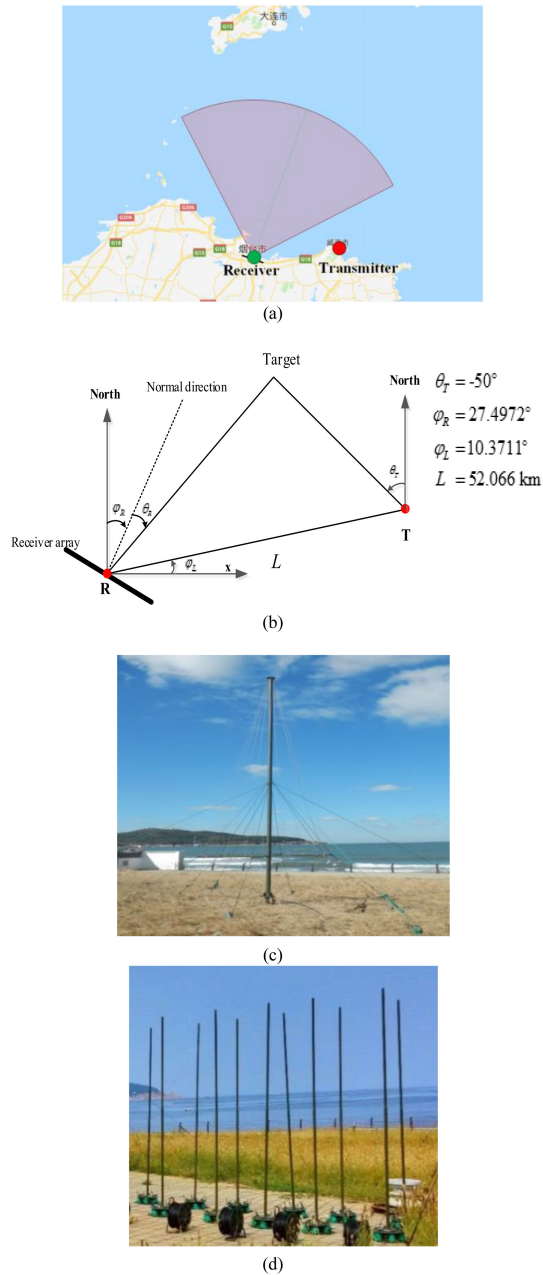


Fig. 10. Layout of the bistatic HFSWR. (a) Location of the transmitter and receiver. (b) Radar system layout scheme. (c) Transmitting antenna. (d) Receiving antenna array.

Compared with microwave radar, HFSWR has coarser azimuth resolution. It can obtain high Doppler resolution or high radial velocity resolution by using long coherent integration. And both the compact HFSWR with small-array and large-array HFSWR can practically achieve the same radial velocity resolution and the same range resolution though they have different azimuth resolution.

In an HFSWR R–D image, a moving ship target is shown as an area target rather than a point target because of the spectrum spread of its echo caused by the variations of its range and velocity during long integration time. For bistatic HFSWR, range refer to range sum $R_T + R_R$. And area targets can provide

more features than point targets or CFAR detection result, which are helpful for distinguishing multiple moving targets.

As can be seen from the previous analysis, the echo spectrum spread of a moving target in a bistatic radar R–D image is more obvious than that of monostatic radar. Therefore, different moving targets can be distinguished from each other in R–D image. For a moving target, its spatial position is constantly changing. And the elliptical velocity and echo amplitude of a nonmaneuvering moving target are also constantly changing basically in two consecutive frames R–D images. So the target detection of the bistatic HFSWR can also be extended in the time domain to achieve integrated detection and tracking, similar to that of a monostatic radar.

Fig. 6 shows a Range–Doppler–time (R–D–T) data of bistatic HFSWR. Fig. 7 shows the range–time (R–T) images and Doppler–time (D–T) image, on which the corresponding AIS tracks were superimposed.

The R–T image illustrates the range change relative to the radar site. The stripes in the image represent the target traces in the R–T domain. The D–T image depicts the variations in the elliptical velocity of the target over time at a fixed range cell. It should be noted that the target trace appears for a short time and then can move to the previous or next range cell in the D–T image, even if the target velocity remains unchanged.

As can be seen from Fig. 7 that the target tracks are clearly seen in both the R–T and D–T images, and they are consistent with the AIS tracks. As each R–T or D–T image is the two-dimensional (2-D) result of the 3-D R–D–T data at a fixed Doppler cell or range cell, respectively, the range cells and Doppler cells where the target is located will actually change with time. As a result, the target track in the radar images and the AIS track do not correspond exactly.

Then, the R–D–T data can be used to track moving targets by integrating detection and tracking. The flow chart of the integrated detection and tracking process for bistatic HFSWR is given in Fig. 8.

Stage 1: R–D–T data construction. Here, R is the range sum for bistatic HFSWR, D is Doppler velocity, which is the elliptical velocity used in the bistatic radar rather than the radial velocity used in the monostatic T/R radar data, and T is frame number. In which, the frame number is related to coherent integration time of each frame T_{CIT} , the interval between each frame ΔT . Here, T_{CIT} can be set between 100 and 300 s to guarantee a sufficient velocity resolution and ΔT can be set as 60 s. When there are many maneuvering ships, values of both T_{CIT} and ΔT should be appropriately reduced. To reduce the time interval of detection results, two consecutive batches of R–D–T data should be overlapped.

Stage 2: Data preprocessing. This stage includes the first-order sea-clutter suppression and CFAR predetection with a low threshold. Compared with a monostatic T/R HFSWR, the characteristics of the frequency shift and the broadening of the first-order sea clutter for a bistatic compact HFSWR makes it more difficult to isolate the first-order sea-clutter spectrum. Equation (3) shows that ∇f_B changes regularly with variation of bistatic angle β . For the beam R–D spectrum of a certain azimuth, the bistatic angle can be calculated according to the

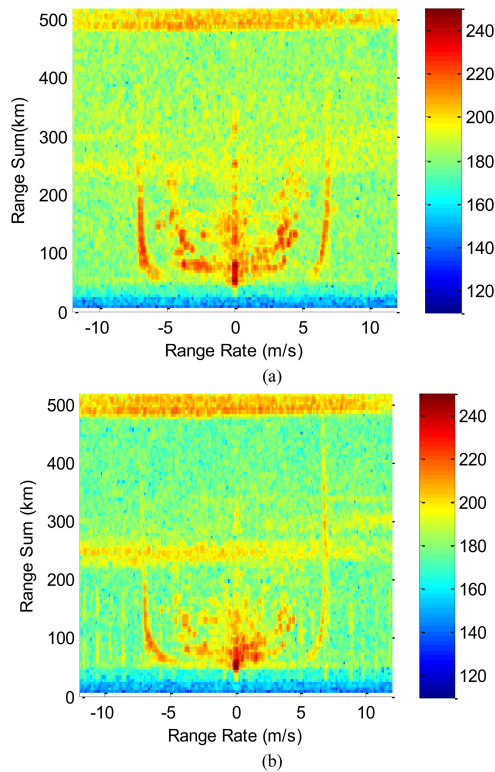


Fig. 11. Typical R-D spectrum of bistatic HFSWR with different beam angles. (a) -48° beam data. (b) 16° beam data.

azimuth and range sum. Therefore, the distance between the left and right first-order spectra of bistatic radar can be calculated. Then a 2-D SNR method can be used to recognize and suppress the first-order sea clutter based on the continuous distribution characteristics of the first-order sea spectrum on each 2-D R-D data. This method was used to extract the first-order sea clutter for high-frequency hybrid sky-surface wave radar [20].

The purpose of CFAR predetection with a low threshold is to extract the possible target with weak signals in advance, which can improve the efficiency of data processing. Although some false targets caused by noise or clutter may exist in a certain frame spectrum, they will be eliminated in the next stage of the integration of detection and tracking because the false targets have different characteristics of temporal and spatial distribution with real targets.

Fig. 9 shows suppression results of the first-order sea clutter and the CFAR predetection results with a low threshold for a given single-frame 2-D R-D spectrum in the 3-D R-D-T data.

As can see from Fig. 6 that the first-order sea clutter of the bistatic HFSWR can be effectively suppressed, and its influence on the target detection has been eliminated. It should be noted that suppression was not achieved for ionospheric clutter over long distances.

Stage 3: Integration of detection and tracking. For stage 3 in Fig. 5, integration of the detection and tracking of the bistatic radar, the dynamic programming method can be used here, and most of the steps are the same as those for a monostatic T/R radar, see details in [3] and [21].

TABLE I
PARAMETERS FOR BISTATIC COMPACT HFSWR

Parameter	Specification
Location of transmitter	Weihai(122.07°E, 37.54°N)
Location of receiver	Yantai (121.49°E, 37.45°N)
Baseline distance	52 km
Waveform	FMICW
Frequency	4.7 MHz
Bandwidth	60 KHz
Element distance	15 m

At the DOA estimation stage, the azimuth of each point in the target track can be estimated using a conventional direction-finding method such as the beam-forming method or the super-resolution direction estimation method. In this article, beam-forming DOA method was used based on its corresponding multiple-channel R-D data. Then, the target's track can be determined using the estimated range and azimuth parameters.

IV. SHIP MONITORING EXPERIMENT AND METHOD EVALUATION

A. Ship Target Monitoring Experiment With Bistatic HFSWR

The experiment was conducted in November 2015 in Shandong, China, and a compact HFSWR with a small array named compact over-horizon radar for marine surveillance was used [19]. The transmitting station was located in Weihai, and the receiving station was located in Yantai City. The transmitter and the receiver were synchronized using GPS time reference over a separation of about 52 km. Fig. 10 shows the locations of the transmitter and receiver, and the photos of its transmitting antenna and receiving antenna array. The key parameters for the radar system are listed in Table I.

The compact HFSWR used a solid-state transmitter with a maximum peak power of 1 kW. The output power of the transmitter could be continuously adjusted. Linear frequency modulated interrupting continuous wave signal was used for the HFSWR. The transmitter antenna transmitted in an omnidirectional pattern, and the antenna's height was 10 m. A higher log-periodic antenna was used to send lower frequency electromagnetic waves. The HF radar receiver is fully digitalized with eight channels. The receiving antenna array of the radar system consists of eight active whip antenna units, each unit equipped with six ground wires. The height of each receiving antenna is 2 m, and it can be deployed easily when setting up the radar site. The receiving antenna array was placed along the coast, with the antennas placed at 15-m intervals.

Fig. 11 shows two R-D spectra measured by the bistatic radar with different beam directions off the boresight. The vertical axis represents half of the range sum R (in km), and the horizontal axis indicates the ellipsoidal velocity relative to the bistatic angle in Hz or in m/s. The measured radar spectra are in good agreement with the simulation results with the same configuration,

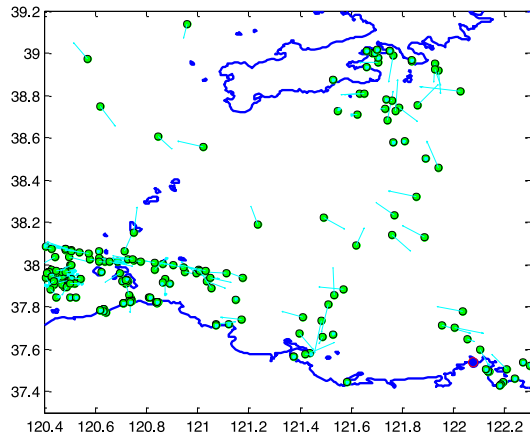


Fig. 12. AIS point distribution at a fixed moment.

TABLE II
AIS INFORMATION OF SHIP T1 AND T2

Symbol	Ship T1	Ship T2
MMSI	413304030	413110000
Name	Jin Ye 588	Bei Hai Jiu 131
Ship type	Cargo ship	Search and rescue ship
Length	95 meter	77 meter
Width	15 meter	14 meter

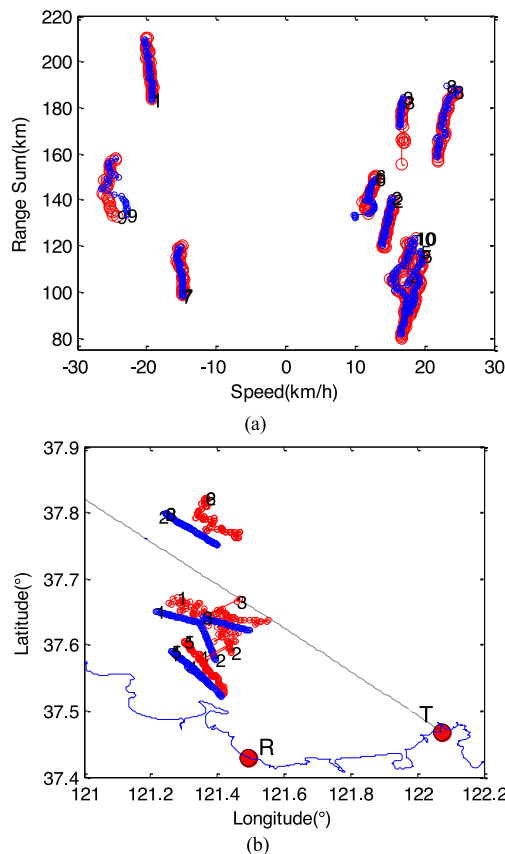


Fig. 13. Partial bistatic HFSWR target tracking results (red circles) and corresponding AIS data (blue circles) recorded during 1 h: (a) in R–D coordinates and (b) in latitude and longitude coordinates.



(a)



(b)

Fig. 14. Photos of ships. (a) Ship T1. (b) Ship T2.¹

shown in Fig. 2. The strongest echo signal appears at the range of about 52 km, which corresponds to the direct signal from the radar transmitter station to the receiving station. The broadening amplitude of the first-order sea clutter of the measured spectra is significantly greater than that of the simulated spectra.

During the experiment, AIS data from the monitored ships was collected and synchronized with the HFSWR data. AIS can provide information such as ship name, ship type, position, heading, and speed, which is often used as ground truth data to validate the detection methods. Fig. 12 shows the processed AIS points and track results in the monitored area.

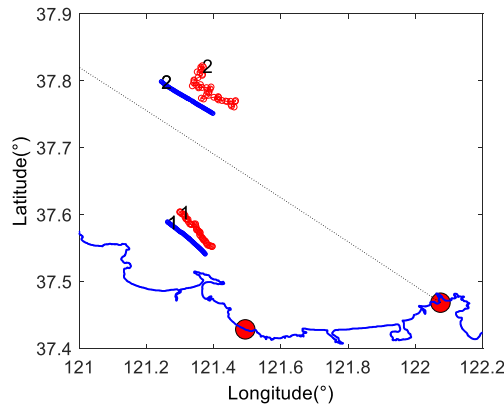
B. Target Monitoring Result Analysis

Fig. 13(a) and (b) shows partial tracking results from the bistatic HFSWR (red circles) and corresponding AIS data (blue circles) recorded during 1 h in the R–D coordinates and latitude and longitude coordinates, respectively.

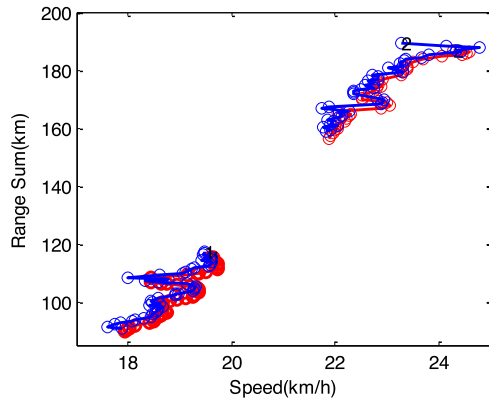
A good match between the target tracking results and the AIS tracks is seen in the R–D coordinate system, while in the lat.–long. coordinate system some deviation exists between the two datasets. It means that the bistatic HFSWR monitoring method can effectively track moving targets. To quantitatively analyze the detection performance of bistatic HFSWR, two examples, Ship T1 and Ship T2, were selected. Table II shows the AIS information for the two ships. And their photos are shown in Fig. 14.

Fig. 15 shows the tracking result of targets T1 and T2 in the lat.–long. coordinates and in the range–velocity coordinates, respectively. The blue curves represent the AIS results and the red curves represent the tracking results of the bistatic HF radar.

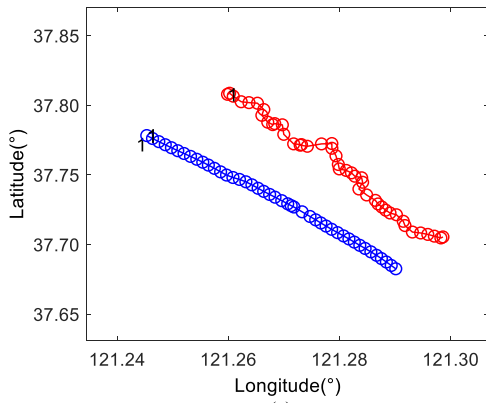
¹[Online]. Available: <http://www.shipxy.com/>



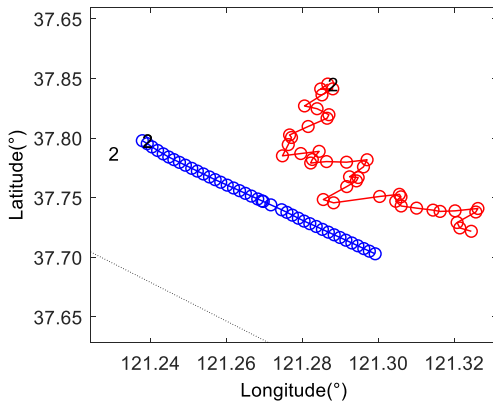
(a)



(b)



(c)



(d)

Fig. 15. Tracking result of the T1 and T2. (a) Tracking results in the latitude and longitude coordinates. (b) Tracking results in the range-velocity coordinates. (c) Enlarged view of the T1 results. (d) Enlarged view of the T2 results.

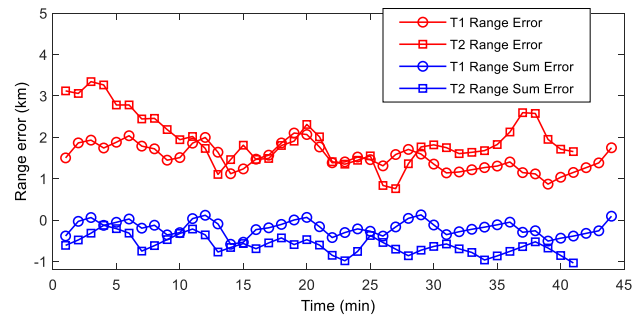


Fig. 16. Range error distribution between the HFSWR and AIS measurements over time for targets T1 and T2 in the two cases.

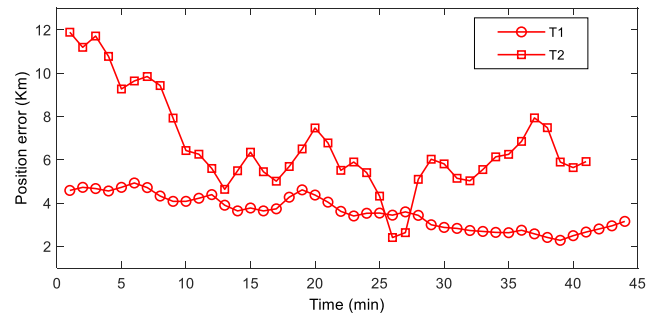


Fig. 17. Position error distribution between the HFSWR and AIS measurements over time for targets T1 and T2 in the two cases.

In the lat.–lon. coordinate plot in Fig. 15, unlike the good match in the R–D coordinate system, the tracking results of the two targets deviate from the AIS data. Because of the large azimuth errors, the distance between the target tracks and the AIS, i.e., position error, is relatively large.

Fig. 16 is the range error distribution curve of two targets and shows the range deviations between the HFSWR and AIS data (blue) over time for the two targets in the bistatic T-R mode (red). The range deviations of the two targets are between 1 and 3 km in the bistatic mode and less than 1 km for range sum, which is equivalent to the case of monostatic T/R mode. These deviations represent the measurement error of the range sum for the bistatic HFSWR. The larger range error for the bistatic radar is mainly due to the presence of a large azimuth error. Correspondingly, the position error of the two targets is relatively large (Fig. 17); most deviations are between 4 and 8 km, reaching up to 12 km. The main reason for such a large position error is that the radar system has a large azimuth error of about 5° . And there is a large system deviation, that is, the mean value of the azimuth error is not 0, which is different from the simulation results.

V. CONCLUSION

In this article, the first-order sea-clutter characteristics and introduced detection blind zone for bistatic HFSWR were investigated. Detection and tracking were integrated in the target monitoring method for bistatic compact HFSWR. The target tracking results using bistatic compact HFSWR were compared with synchronized AIS data to verify the accuracy of the tracking

results and the effectiveness of the monitoring method. Moreover, a preliminary statistical analysis was conducted to evaluate the position accuracy of the target detection of the bistatic compact HF/SWR from simulation analysis and comparison of the results with the experimental data. The analysis shows that bistatic radars have larger errors than monostatic T/R radars, with a position error as large as 10 km. Therefore, the influence of the spatial position accuracy of different radar configurations on the detection results should be considered in the association and fusion process of multistation network observation systems.

Future article will focus on detailed analysis of position accuracy for bistatic compact HF radars and comparative analysis with monostatic T/R radars.

ACKNOWLEDGMENT

The authors thank the anonymous reviewers for their comments and suggestions that have helped to improve the quality and the readability of this article. The authors thank Dalia Lahav-Jones, from Liwen Bianji, Edanz Group China², for editing the English text of a draft of this article.

REFERENCES

- [1] A. M. Ponsford, "Surveillance of the 200 nautical mile exclusive economic zone (EEZ) using high frequency surface wave radar (HFSWR)," *Can J. Remote Sens.*, vol. 27, no. 4, pp. 354–360, 2001.
- [2] Y. T. Liu, R. Q. Xu, and N. Zhang, "Progress in HFSWR research at Harbin Institute of Technology," in *Proc. Int. Conf. Radar*, Sep. 2003, pp. 522–528.
- [3] Y. G. Ji, J. Zhang, Y. M. Wang, W. F. Sun, and M. Li, "Target monitoring using small-aperture compact high-frequency surface wave radar," *IEEE Aerosp. Electron. Syst. Mag.*, vol. 33, no. 3, pp. 22–31, Mar. 2018.
- [4] D. B. Trizna, "A bistatic HF radar for current mapping and robust ship tracking," in *Proc. Oceans*, Sep. 2008, pp. 1–6.
- [5] S. J. Anderson, P. J. Edwards, P. Marrone, and Y. I. Abramovich, "Investigations with SECAR—A bistatic HF surface wave radar," in *Proc. Int. Conf. Radar*, 2003, pp. 717–722.
- [6] J. H. Xie, B. Li, Y. B. Chou, and N. Zhang, "Ship detection range of T/R-R high frequency surface wave radar," *Chin. J. Radio Sci.*, vol. 25, no. 2, pp. 234–239, 2010.
- [7] P. Marrone and P. Edwards, "The case for bistatic HF surface wave radar," in *Proc. Int. Conf. Radar*, Sep. 2008, pp. 633–638.
- [8] W. F. Sun, Z. Z. Pang, W. M. Huang, Y. G. Ji, and Y. S. Dai, "Vessel velocity estimation and tracking from doppler echoes of t/r-r composite compact HFSWR," *IEEE J. Sel. Topics Appl. Earth Observ. Remote Sens.*, vol. 14, pp. 4427–4440, Apr. 2021.
- [9] Z. Hua, C. J. Yu, G. J. Zhou, and T. F. Quan, "Track initiation in monostatic-bistatic composite high frequency surface wave radar network based on NFE model," in *Proc. Int. Conf. Electron. Inf. Eng.*, Aug. 2010, pp. 81–85.
- [10] K. R. Zhao, C. Yu, G. Zhou, and T. Quan, "Simultaneous target flying mode identification and altitude estimation in bistatic T/R-R HFSWR," *Asian J. Control*, vol. 18, no. 3, pp. 1062–1074, 2016.
- [11] H. Leong, "The potential of bistatic HF surface wave radar system for the surveillance of water-entry area along coastline," in *Proc. IEEE Conf. Radar*, Apr. 2006, pp. 24–27.
- [12] J. H. Xie, M. L. Sun, and Z. Y. Ji, "Space-time model of the first-order sea clutter in onshore bistatic high frequency surface wave radar," *IET Radar Sonar Navig.*, vol. 9, no. 1, pp. 55–61, 2015.
- [13] J. Wang, R. Dizaji, and A. Ponsford, "Analysis of clutter distribution in bistatic high frequency surface wave radar," in *Proc. Can. Conf. Elect. Comput. Eng.*, 2004, pp. 1301–1304.
- [14] J. Yang, B. Wen, C. Zhang, X. Huang, Z. Yan, and W. Shen, "A bistatic HF radar for surface current mapping," *IEICE Electron. Exp.*, vol. 7, no. 19, pp. 1435–1440, 2010.
- [15] E. Gill and J. Walsh, "High frequency bistatic cross section of the ocean surface," *Radio Sci.*, vol. 36, no. 6, pp. 1459–1476, 2001.
- [16] K. Gurgel, A. Dzvonkovskaya, T. Pohlmann, T. Schlick, and E. Gill, "Simulation and detection of tsunami signatures in ocean surface currents measured by HF radar," *Ocean Dyn.*, vol. 61, no. 10, pp. 1495–1507, 2011.
- [17] T. Tsao, M. Slamani, P. Varshney, D. Weiner, H. Schwarzlander, and S. Borek, "Ambiguity function for a bistatic radar," *IEEE Trans. Aerosp. Electron. Syst.*, vol. 33, no. 3, pp. 1041–1051, Jul. 1997.
- [18] Y. He, G. H. Wang, J. J. Xiu, and J. H. Xiu, "Redundant data compression and location accuracy analysis in T/R-R bistatic radar system," in *Proc. 16th World Comput. Congr. 5th Int. Conf. Signal Process.*, 2000, pp. 1951–1955.
- [19] Y. G. Ji et al., "A small array HFSWR system for ship surveillance," in *Proc. IET Int. Radar Conf.*, Oct. 2015, pp. 14–16.
- [20] Y. G. Ji, J. Zhang, X. L. Chu, Y. M. Wang, and L. Q. Yang, "Ocean surface current measurement with high-frequency hybrid sky-surface wave radar," *Remote Sens. Lett.*, vol. 8, no. 7, pp. 617–626, 2017.
- [21] J. Arnold, S. W. Shaw, and H. Pasternack, "Efficient target tracking using dynamic programming," *IEEE Trans. Aerosp. Electron. Syst.*, vol. 29, no. 1, pp. 44–56, Jan. 1993.



Yonggang Ji (Member, IEEE) received the B.S. and M.S. degrees in electronic engineering from the Ocean University of China, Qingdao, China, in 2001 and 2003, respectively, and the Ph.D. degree in physical oceanography from the Institute of Oceanology, Chinese Academy of Sciences, Qingdao, China, in 2006.

He is currently a Professor with the College of Oceanography and Space Informatics, China University of Petroleum (East China), Qingdao, China.

His research interests include high-frequency surface wave radar and applications, compact high frequency over the horizon radar system, marine target monitoring with multiple remote sensors, remote sensing of sea state, and ocean remote sensing.

Prof. Ji is a senior member of the Chinese Institute of Electronics. He was the recipient of the Outstanding Contribution Award from the China–EU development cooperation program, and the Technological Progress Award from SOA.



Yiming Wang (Member, IEEE) received the B.S. degree (Hons.) in electrical and electronic engineering from Nanyang Technology University, Singapore, in 2008, the M.S. degree in communication engineering from National University of Singapore, Singapore, in 2010, and the Ph.D. degree in information and communication engineering from the Harbin Institute of Technology, Harbin, China, in 2021.

He is currently an Associate Professor with the First Institute of Oceanography, Ministry of Natural Resources, China. His research interests include

high-frequency surface wave radar and its applications, clutter and interference suppression, target detection, and array signal processing.



Weifeng Sun (Member, IEEE) received the B.Eng. degree in communication engineering and the Ph.D. degree in signal and information processing from Shandong University, Jinan, China, in 2005 and 2010, respectively.

He is currently an Associate Professor with the College of Oceanography and Space Informatics, China University of Petroleum (East China), Qingdao, China. From 2018 to 2019, he was a Visiting Scholar with the Memorial University of Newfoundland, St. John's, NL, Canada. His research interests

include marine target detection and tracking via compact high-frequency surface wave radar, and image processing.

²[Online]. Available: www.liwenbianji.cn/ac



Ruifu Wang received the Ph.D. degree in GIS and remote sensing from the Ocean University of China, Qingdao, China, in 2006.

He is currently an Associate Professor with the College of Geomatics, SDUST, Qingdao, China. His research interests include marine GIS and remote sensing of sea ice.



Xiaoyu Cheng received the B.Eng. degree in software engineering from the China University of Petroleum (East China), Qingdao, China, in 2020. He is currently working toward the M.Eng. degree in electronic information with the College of Oceanography and Space Informatics, China University of Petroleum (East China), Qingdao, China.

His research interests include motion compensation and signal processing for shipborne high-frequency ground wave radar.



Ming Li was born in Hefei, China, in 1975. He received the B.S. and Ph.D. degrees in control theory and control engineering from the Northeastern University, Shenyang, China, in 1997 and 2003, respectively.

From 2003 to 2006, he was with the Electric Automation Institute, Northeastern University, as a Postdoctoral Fellow. In 2006, he joined the College of Engineering, Ocean University of China, Qingdao, China. Since 2013, he has been a Full Professor with the Automation and Measurement Department,

Ocean University of China. He has authored three books, more than 40 articles, and more than ten inventions. His research interests include intelligent signal processing and its application in HFSWR, ocean instrument and equipment development, and ocean energy power system modeling and control.



Xu Liang received the B.Eng. degree in electronic and information engineering from the Shandong University of Science and Technology, Qingdao, China, in 2020. He is currently working toward the M.Eng. degree in electronic information with the College of Ocean and Spatial Information, China University of Petroleum (East China), Qingdao, China.

His research interests include the ocean echo mechanism and remote sensing of sea state with shipborne bistatic high-frequency surface wave radar.